# Research on the Behaviour of a Toroidal LPG Storage Tank under Uniaxial Traction Loads

Assistant professor PhD. Eng. **Petre OPRIŢOIU**[1,*]

[1] Technical University of Cluj-Napoca, Department of MTC, Observatorului Street, no. 72-74, Cluj-Napoca, 400363, Cluj county, Romania.

* petre.opritoiu@mtc.utcluj.ro

***Abstract:*** *A numerical model has been developed to reproduce the uniaxial traction loads on the three-dimensional (3-D) geometry of a hexagonal toroid with regular hexagonal cross-section used in the manufacturing of liquefied petroleum gas (LPG) storage tanks from the automotive industry. Several numerical applications are presented, with an optimization procedure, addressing the influence of affecting factors (temperature, corrosion and traction loads). Internal state stress and strains were also modeled using the finite-element method (FEM). The obtained results highlight the effectiveness of the proposed approach in correlating LPG) storage tank structure with external traction loads. The relationship between the strains, stresses, and the applied traction load noticeably deviates from linearity. This approach based on the FEM method can improve the simulation accuracy and to fully explore the design parameters (size, weight, shape, materials, mechanical properties, etc.) of the product early in the development process, while greatly reduce the computing cost.*

***Keywords:*** *3-D hexagonal toroidal LPG fuel tank, automotive industry, industrial engineering design, optimization methods*

## 1. Introduction

Over the past two decades, the current reality of the global competitive market has forced many companies to apply Computer-aided design (CAD) / Computer-aided manufacturing (CAM) systems [1-3] to become more efficient and to develop innovative solutions [4-6], in manufacturing of a high-quality product [7-9].

In storage tanks, manufacturing a well-designed production process based on the optimization techniques is applied to increase productivity and improve quality [10, 11].

To simulate complex parametric models of storage tanks [12-14], which work under different operating conditions, in an industrially acceptable time, various dedicated parametric modeling software [15-17], with a high level of flexibility and adaptability, are used [18-20].

From an industrial standpoint, the feature-based parametric CAD is currently the industry standard technology to create geometric models and assemblies and is used in the manufacturing of LPG storage tanks from the automotive industry [21-23].

Problems related to modeling strategies of LPG storage tanks, identifying the most appropriate modeling practice for a particular design situation and understanding how the design tree can be structured are major factors to guarantee success and to ensure an efficient functional model and to minimize the time and effort in the design process [24-26].

Various variants of LPG storage tanks with good technical-functional characteristics can be designed using virtual prototypes with specific modeling procedures, based on descriptive geometry concepts [27-29], and formal CAD strategies for creating robust and reusable parametric CAD models with a lower cost of production [30, 31].

Finite element analysis (FEA) is a computer-based process used for modeling complex products [32-34] and failure analysis which provides various advantages to complement laboratory experiments finding a series of solutions to engineering complex problems [35-37].

In the scientific literature, there are proposed for the design and improvement of these storage tanks different CFD (Computational Fluid Dynamics) models that could be used as a flexible modelling tool in CFD simulations. The life of LPG storage tank is determined by a number of variables such as the load efforts, position, mass, the tank material, the corrosion process etc.

This paper studies the influence of uniaxial traction loads applied normally on the parallel sides of the 3-D hexagonal toroid with regular hexagonal cross-section used in the manufacturing of LPG storage tanks using the finite element analysis.

## 2. Design methodology

### 2.1. Basic geometry of the parametric 3-D model

Let's consider the parametric 3-D model generated by revolving of a closed generating curve $C_G$ (a hexagon with rounded corners) along a closed guiding curve $C_D$ (a hexagon with rounded corners) as shown in figs. 1 and 2 [14].
The following parameters were applied as input parameters to the 3-D parametric model (figs. 1 and 2): a) a closed generating curve CG (a hexagon with a side value L = 175 mm, with rounded corners, radius R = 50 mm), and b), the guiding curve CD (a hexagon with a side value L = 430 mm, with rounded corners, radius R = 180 mm), and the thickness = 10 mm.

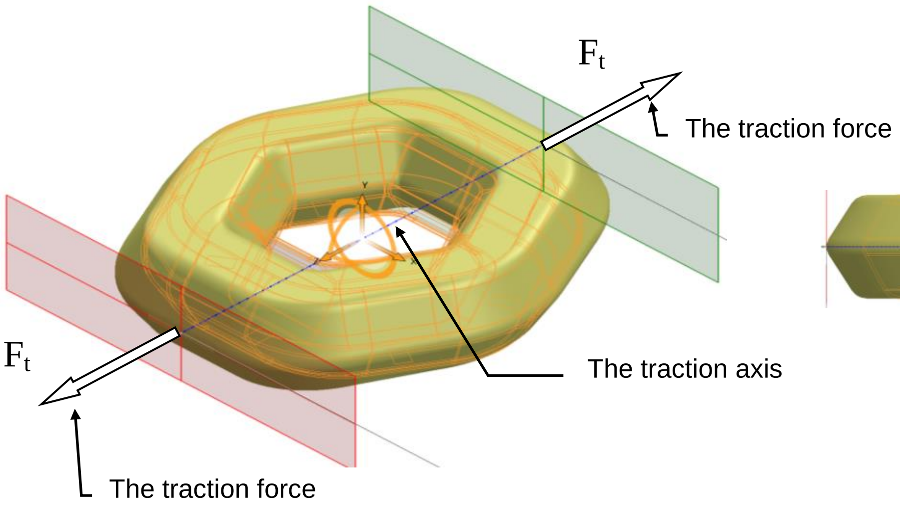


**Fig. 1.** The isometric representation of 3-D model, not deformed, before the uniaxial traction

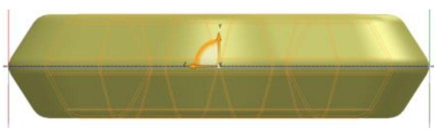

**Fig. 2.** The lateral representation of 3-D model not deformed, before the uniaxial traction

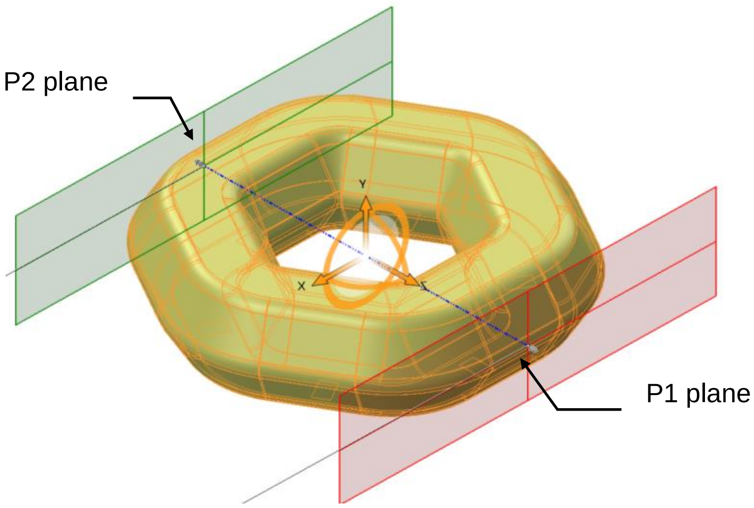


**Fig. 3.** The isometric representation of 3-D model, deformed, after the uniaxial traction

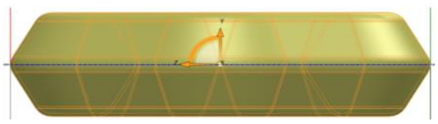

**Fig. 4.** The lateral representation of 3-D model deformed, after the uniaxial traction

The deformation of the shape of the 3-D model is made as a result of the displacement of the point of application of force over a distance $\Delta L_t$ = 1.33% from the value of the median diameter of the model measured in the direction of the traction axis.

As a result of the applied forces, a decrease of the cross-sectional area appears, simultaneously with the elongation of the shape of the model in the forces direction.
The uniaxial displacement under traction loads is noted with $L_c$.

### 2.2. Numerical analysis of the parametric 3-D model

Based on the physical model, the modeling was done in the AutoCAD Autodesk 2020 software and the numerical analysis was performed with SolidWorks 2020 software with the Static, Thermal and Design Study modules. The design data used were:

- the tank material is AISI 4340 steel;
- the maximum hydraulic test pressure: $p_{max}$ = 30 bar;
- the working temperature between the limits: T = -30 $^0$C up to T = 60 $^0$C;
- supporting surfaces located on the inferior side;
- the duration of the tank exploitation: $n_a$ = 15 years;
- the corrosion rate of the material: $v_c$ = 0.07 mm/year.

Numerical calculations were performed for: mesh standard type, solid mesh, curvature-based mesh with quality high, Jacobian in 16 points, element size 11 mm, number of nodes 30628, number of elements 15368.
The parameterized 3-D model used in calculus is a section of ½ (fig. 5) from the initial physical model and the corresponding surfaces to which the constraints and restrictions are applied are shown in fig. 5. The finite element discretization for the 3-D parametric model is shown in fig. 6.

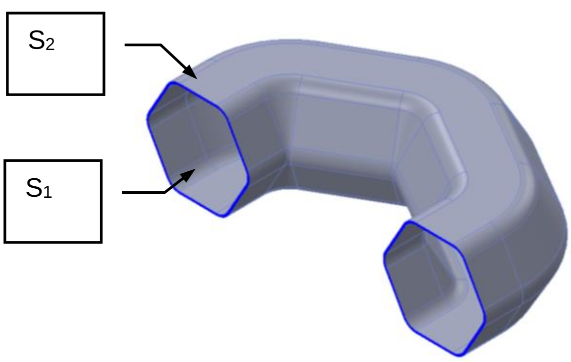


**Fig. 5.** The surfaces to which the constraints were applied.

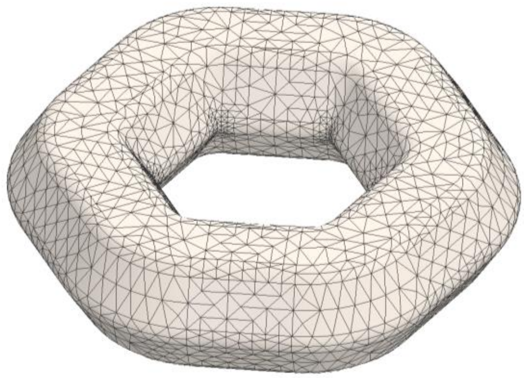

**Fig. 6.** The discretization of the model

The design data used in this analysis for the tank lateral cover are:
- the maximum pressure $p_{max}$ = 3 N/mm$^2$ on the inner surface $S_1$;
- the working temperature between the limits: T = -30 $^0$C to T = 60 $^0$C on the exterior surface $S_2$;
- the fixation of the tank on the six tank supports located at the inferior part of the tank.
The values of the state of stress Von Mises determined by the finite element method for $n_a$ = 0, 5, 10 and 15 years are shown in table 1.

**Table 1:** The Von Misess resultant effort for $n_a$= 0, 5, 10 and 15 years

| Lc [mm] | T [$^0$C] | | | | T [$^0$C] | | | |
|---|---|---|---|---|---|---|---|---|
| | -30$^0$ | 0$^0$ | 30$^0$ | 60$^0$ | -30$^0$ | 0$^0$ | 30$^0$ | 60$^0$ |
| | $n_a$ = 0 [years] | | | | $n_a$ = 5 [years] | | | |
| | $\sigma_t$ [MPa] | | | | $\sigma_t$ [MPa] | | | |
| 0 | 665.40 | 565.66 | 479.29 | 527.43 | 610.22 | 514.24 | 511.09 | 560.58 |
| 1 | 545.22 | 470.35 | 485.68 | 541.97 | 593.51 | 502.09 | 506.01 | 563.14 |
| 2 | 505.58 | 443.67 | 466.81 | 527.46 | 534.81 | 472.72 | 510.20 | 556.49 |
| 3 | 521.01 | 448.29 | 487.10 | 540.16 | 584.30 | 502.98 | 514.43 | 571.78 |
| 4 | 531.82 | 457.71 | 473.33 | 527.49 | 546.24 | 474.59 | 525.31 | 588.70 |
| 5 | 529.59 | 455.52 | 488.13 | 546.48 | 565.15 | 486.81 | 500.36 | 558.24 |
| 6 | 524.46 | 492.94 | 474.49 | 531.09 | 602.07 | 524.28 | 521.33 | 578.30 |

| | | | | | | | | |
|---|---|---|---|---|---|---|---|---|
| 7 | 657.82 | 559.64 | 485.78 | 538.97 | 576.45 | 494.93 | 478.15 | 522.33 |
| 8 | 619.07 | 524.38 | 468.05 | 468.05 | 704.33 | 604.23 | 505.07 | 559.88 |
| 9 | 523.90 | 446.61 | 466.19 | 521.03 | 691.79 | 591.13 | 502.17 | 556.59 |
| 10 | 522.72 | 444.74 | 470.08 | 527.07 | 589.18 | 514.04 | 507.66 | 568.22 |
| | $n_a$ = 10 [years] | | | | $n_a$ = 15 [years] | | | |
| 0 | 716.26 | 615.97 | 591.97 | 641.72 | 754.50 | 655.70 | 636.94 | 688.12 |
| 1 | 718.61 | 623.72 | 586.50 | 632.99 | 680.88 | 589.79 | 591.14 | 638.86 |
| 2 | 585.76 | 509.56 | 535.62 | 587.22 | 760.61 | 669.24 | 628.56 | 679.21 |
| 3 | 591.81 | 516.25 | 567.98 | 623.54 | 657.33 | 583.00 | 643.56 | 708.33 |
| 4 | 722.39 | 623.49 | 525.83 | 545.65 | 640.55 | 566.19 | 600.51 | 644.61 |
| 5 | 602.64 | 531.32 | 576.29 | 642.99 | 660.04 | 586.78 | 622.83 | 658.88 |
| 6 | 737.04 | 738.28 | 740.10 | 742.49 | 602.60 | 572.32 | 634.55 | 700.08 |
| 7 | 587.54 | 510.56 | 528.33 | 559.51 | 636.33 | 567.02 | 565.91 | 573.71 |
| 8 | 683.04 | 585.06 | 555.56 | 609.76 | 695.16 | 592.73 | 556.54 | 591.79 |
| 9 | 584.59 | 509.34 | 584.59 | 585.40 | 789.42 | 683.81 | 579.95 | 597.50 |
| 10 | 581.63 | 505.67 | 511.08 | 561.02 | 735.27 | 637.78 | 542.83 | 590.54 |

The graphs corresponding to the Von Mises resultant efforts $\sigma_t$ ($L_c$, T) taking into account the results from table 1 are graphically shown in figs. 7-10, respectively.

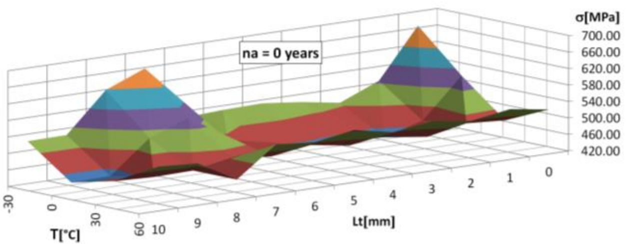


**Fig. 7.** The graphs of $\sigma = f(L_c, T)$ for $n_a$ = 0 years

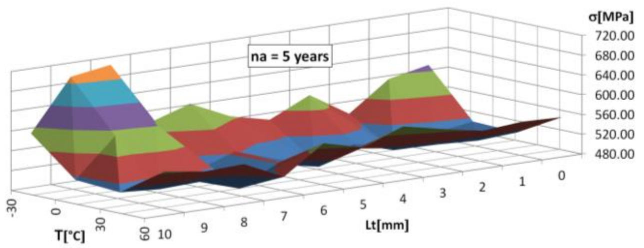


**Fig. 8.** The graphs of $\sigma = f(L_c, T)$ for $n_a$ = 5 years

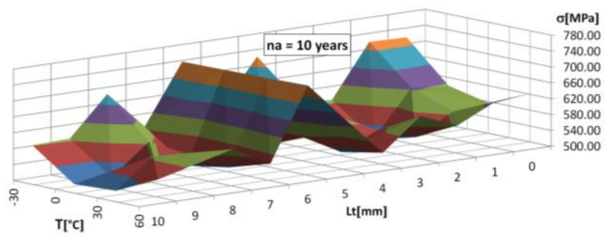


**Fig. 9.** The graphs of $\sigma = f(L_c, T)$ for $n_a$ = 10 years

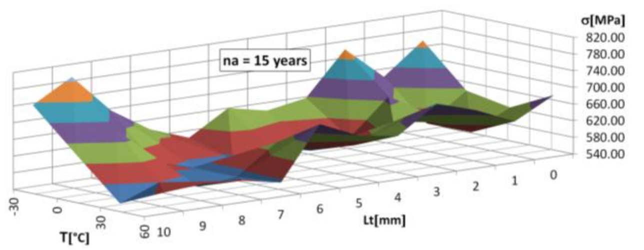


**Fig. 10.** The graphs of $\sigma = f(L_c, T)$ for $n_a$ = 15 years

The graphs of curves corresponding to the Von Mises resultant efforts $\sigma_t$ ($L_c$, T) for $n_a$ = {0, 5, 10, and 15 years}, are graphically shown in fig. 11.

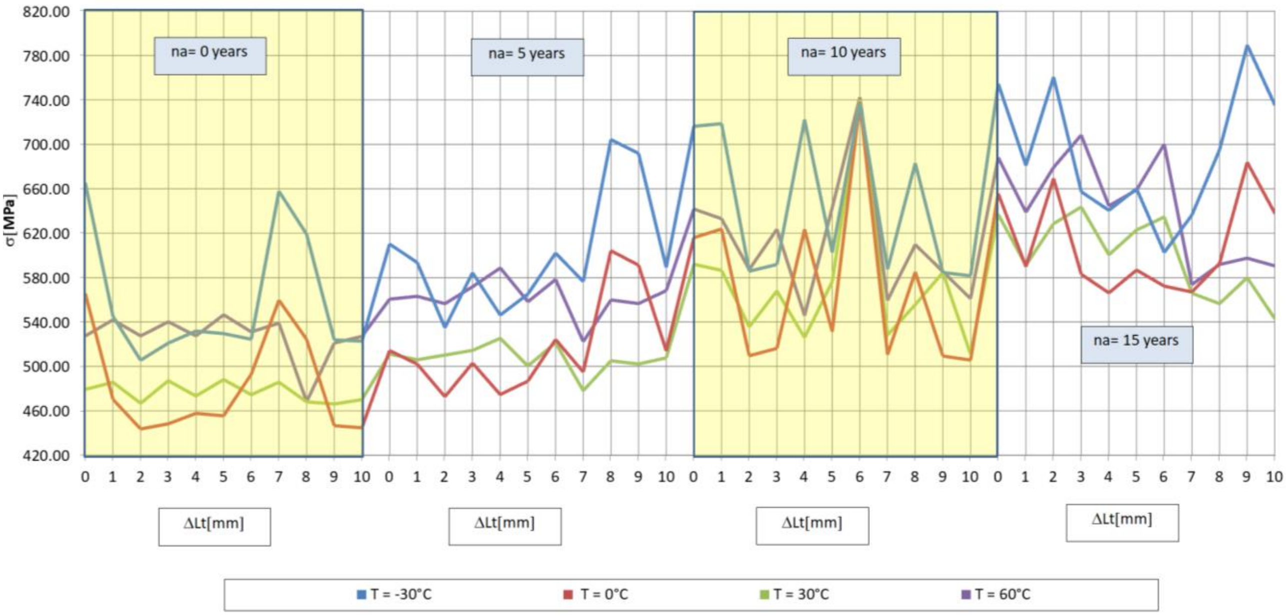


**Fig. 11.** The graphs of $\sigma_t$ ($L_c$, T) for: T = {-30 $^0$C, 0 $^0$C, 30 $^0$C, 60 $^0$C} and $n_a$= {0, 5, 10 and 15 years}

The results show the Von Mises resultant efforts has a maximum value corresponding for T = -30 $^0$C. It was calculated the percentage variation of the Von Mises effort $\Delta\sigma_t$ ($L_c$, T) versus the resulting stress state of the non-deformed tank (for $L_c$ = 0), using the following formula:

$$\Delta\sigma_t = \frac{(\sigma_{Lc=0} - \sigma)}{\sigma_{Lc=0}} \cdot 100\ [\%] \quad (1)$$

The percentage variation of Von Mises resultant effort $\Delta\sigma_t$ in relation to the initial effort status (computed in table 2) and the corresponding graphs (in 2-D) are shown in fig. 12, while the corresponding graphs (in 3-D) are shown in figs. 13-16.

**Table 2:** The percentage variation of Von Mises resultant effort for $n_a$= 0, 5, 10 and 15 years

| Lc [mm] | T [$^0$C] | | | | T [$^0$C] | | | |
|---|---|---|---|---|---|---|---|---|
| | -30$^0$ | 0$^0$ | 30$^0$ | 60$^0$ | -30$^0$ | 0$^0$ | 30$^0$ | 60$^0$ |
| | $n_a$ = 0 [years] | | | | $n_a$ = 5 [years] | | | |
| | $\Delta\sigma_t$ [%] | | | | $\Delta\sigma_t$ [%] | | | |
| 1 | -18.06 | -16.85 | 1.33 | 2.76 | -2.74 | -2.36 | -0.99 | 0.46 |
| 2 | -24.02 | -21.57 | -2.60 | 0.01 | -12.36 | -8.07 | -0.18 | -0.73 |
| 3 | -21.70 | -20.75 | 1.63 | 2.41 | -4.25 | -2.19 | 0.65 | 2.00 |
| 4 | -20.08 | -19.08 | -1.24 | 0.01 | -10.49 | -7.71 | 2.78 | 5.02 |
| 5 | -20.41 | -19.47 | 1.84 | 3.61 | -7.39 | -5.33 | -2.10 | -0.42 |
| 6 | -21.18 | -12.86 | -1.00 | 0.69 | -1.34 | 1.95 | 2.00 | 3.16 |
| 7 | -1.14 | -1.06 | 1.35 | 2.19 | -5.54 | -3.76 | -6.44 | -6.82 |
| 8 | -6.96 | -7.30 | -2.34 | -11.26 | 15.42 | 17.50 | -1.18 | -0.12 |
| 9 | -21.27 | -21.05 | -2.73 | -1.21 | 13.37 | 14.95 | -1.75 | -0.71 |
| 10 | -21.44 | -21.38 | -1.92 | -0.07 | -3.45 | -0.04 | -0.67 | 1.36 |
| | $n_a$ = 10 [years] | | | | $n_a$ = 15 [years] | | | |
| | $\Delta\sigma_t$ [%] | | | | $\Delta\sigma_t$ [%] | | | |
| 1 | 0.33 | 1.26 | -0.92 | -1.36 | -9.76 | -10.05 | -7.19 | -7.16 |
| 2 | -18.22 | -17.27 | -9.52 | -8.49 | 0.81 | 2.06 | -1.32 | -1.30 |
| 3 | -17.38 | -16.19 | -4.05 | -2.83 | -12.88 | -11.09 | 1.04 | 2.94 |
| 4 | 0.85 | 1.22 | -11.17 | -14.97 | -15.10 | -13.65 | -5.72 | -6.32 |

| | | | | | | | | |
|---|---|---|---|---|---|---|---|---|
| 5 | -15.86 | -13.74 | -2.65 | 0.20 | -12.52 | -10.51 | -2.21 | -4.25 |
| 6 | 2.90 | 19.86 | 25.02 | 15.70 | -20.13 | -12.72 | -0.37 | 1.74 |
| 7 | -17.97 | -17.11 | -10.75 | -12.81 | -15.66 | -13.52 | -11.15 | -16.63 |
| 8 | -4.64 | -5.02 | -6.15 | -4.98 | -7.87 | -9.60 | -12.62 | -14.00 |
| 9 | -18.38 | -17.31 | -1.25 | -8.78 | 4.63 | 4.29 | -8.95 | -13.17 |
| 10 | -18.80 | -17.91 | -13.66 | -12.58 | -2.55 | -2.73 | -14.78 | -14.18 |

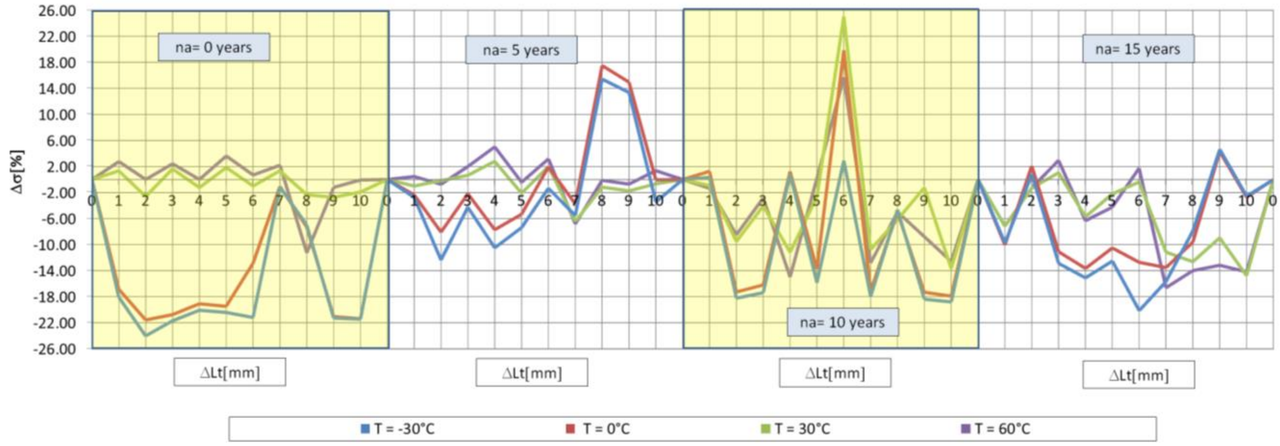


**Fig. 12.** The graphs of Δσ ($L_c$, T) for: T = {-30 $^0$C, 0 $^0$C, 30 $^0$C, 60 $^0$C } and $n_a$= {0, 5, 10 and 15 years}

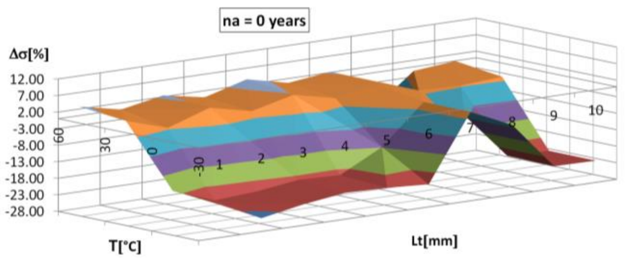


**Fig. 13.** The graphs of Δσ ($L_c$, T) for $n_a$ = 0 years

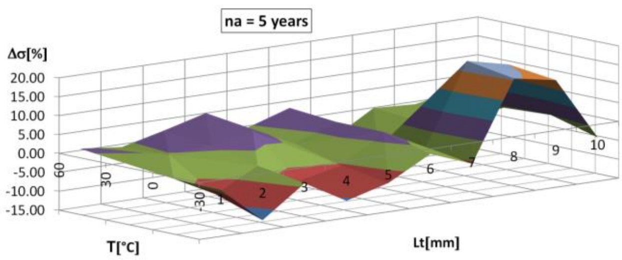


**Fig. 14.** The graphs of Δσ ($L_c$, T) for $n_a$ = 5 years

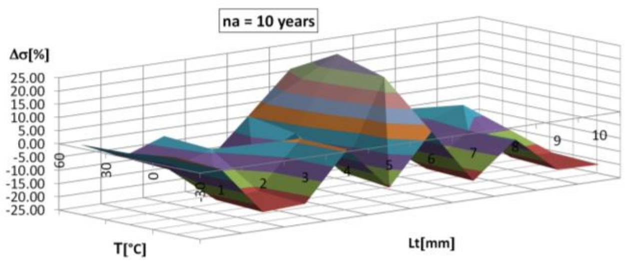


**Fig. 15.** The graphs of Δσ ($L_c$, T) for $n_a$ = 10 years

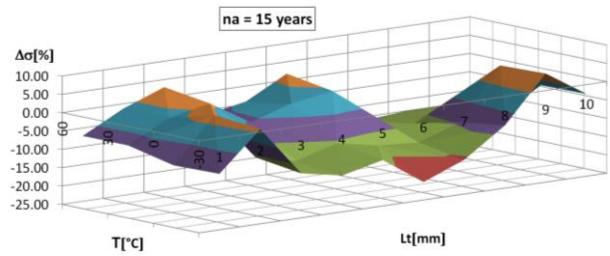


**Fig. 16.** The graphs of Δσ ($L_c$, T) for $n_a$ = 15 years

For the most important cases of the uniaxial traction loads, the Von Mises resultant efforts $\sigma_t$ ($L_c$, T) was calculated taking into account the results from table 3, while the corresponding graphs are shown in figs. 17-20.

**Table 3:** The particular cases for graphical representation of the Von Mises resultant effort

| No. case | $n_a$ [years] | Lc [mm] | T [°C] | $\sigma_t$ [MPa] | u [mm] |
|---|---|---|---|---|---|
| 1 | 0 | 8 | -30 | 468.05 | 0.598 |
| 2 | 5 | 6 | 0 | 524.28 | 0.682 |
| 3 | 10 | 6 | 30 | 740.10 | 0.741 |
| 4 | 15 | 4 | 60 | 644.61 | 0.849 |

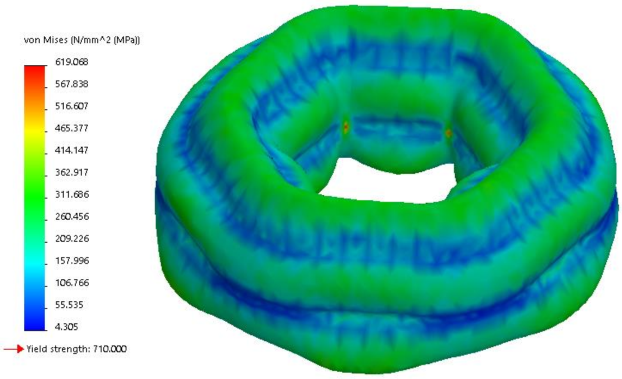


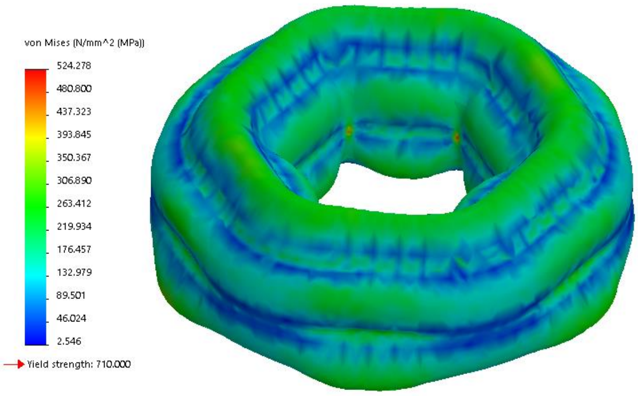


**Fig. 17.** The graphs of $\sigma = f(L_c, T)$ for case 1 **Fig. 18.** The graphs of $\sigma = f(L_c, T)$ for case 2

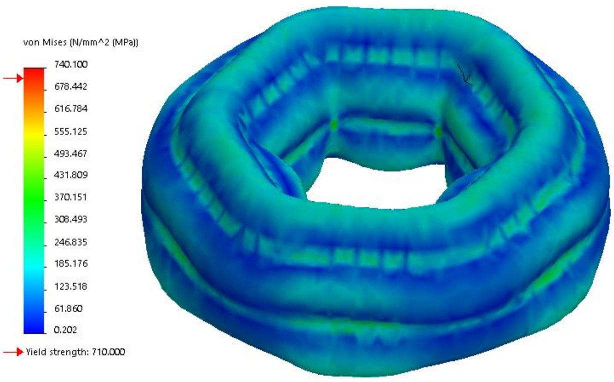


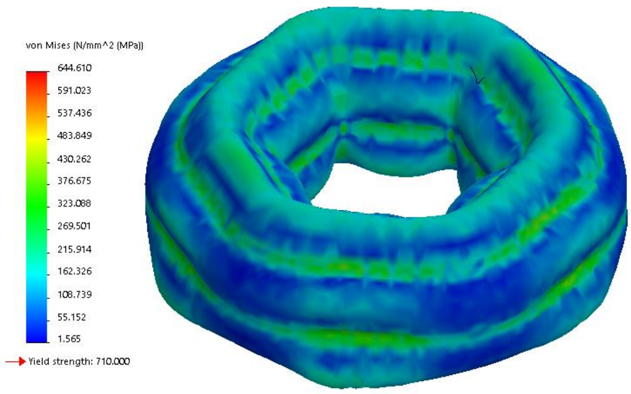


**Fig. 19.** The graphs of $\sigma = f(L_c, T)$ for case 3 **Fig. 20.** The graphs of $\sigma = f(L_c, T)$ for case 4

The values of the resultant linear deformation *u* determined by the finite element method for $n_a$= {0, 5, 10 and 15 years} are shown in table 4.

**Table 4:** The resultant linear deformation for $n_a$= {0, 5, 10 and 15 years}

| Lc [mm] | T [$^0$C] | | | | T [$^0$C] | | | |
|---|---|---|---|---|---|---|---|---|
| | -30$^0$ | 0$^0$ | 30$^0$ | 60$^0$ | -30$^0$ | 0$^0$ | 30$^0$ | 60$^0$ |
| | $n_a$ = 0 [years] | | | | $n_a$ = 5 [years] | | | |
| | $u_c$ [mm] | | | | $u_c$ [mm] | | | |
| 0 | 0.869 | 0.837 | 0.805 | 0.777 | 0.938 | 0.904 | 0.871 | 0.841 |
| 1 | 0.652 | 0.660 | 0.671 | 0.685 | 0.709 | 0.715 | 0.724 | 0.733 |
| 2 | 0.596 | 0.603 | 0.612 | 0.622 | 0.675 | 0.683 | 0.693 | 0.705 |
| 3 | 0.619 | 0.628 | 0.638 | 0.651 | 0.672 | 0.678 | 0.686 | 0.695 |
| 4 | 0.622 | 0.631 | 0.642 | 0.656 | 0.700 | 0.711 | 0.723 | 0.736 |
| 5 | 0.624 | 0.628 | 0.634 | 0.641 | 0.685 | 0.692 | 0.700 | 0.711 |
| 6 | 0.618 | 0.626 | 0.637 | 0.650 | 0.675 | 0.682 | 0.691 | 0.703 |
| 7 | 0.618 | 0.624 | 0.634 | 0.646 | 0.644 | 0.636 | 0.632 | 0.639 |

| | | | | | | | | |
|---|---|---|---|---|---|---|---|---|
| 8 | 0.598 | 0.604 | 0.611 | 0.611 | 0.671 | 0.679 | 0.689 | 0.700 |
| 9 | 0.602 | 0.609 | 0.617 | 0.629 | 0.698 | 0.701 | 0.707 | 0.713 |
| 10 | 0.614 | 0.621 | 0.631 | 0.642 | 0.699 | 0.703 | 0.710 | 0.717 |
| | $n_a$ = 10 [years] | | | | $n_a$ = 15 [years] | | | |
| 0 | 1.011 | 0.974 | 0.944 | 0.916 | 1.106 | 1.076 | 1.047 | 1.020 |
| 1 | 0.840 | 0.842 | 0.845 | 0.851 | 0.872 | 0.869 | 0.867 | 0.794 |
| 2 | 0.711 | 0.715 | 0.721 | 0.729 | 0.788 | 0.791 | 0.797 | 0.805 |
| 3 | 0.737 | 0.748 | 0.761 | 0.776 | 0.777 | 0.787 | 0.799 | 0.812 |
| 4 | 0.731 | 0.729 | 0.735 | 0.743 | 0.834 | 0.837 | 0.842 | 0.849 |
| 5 | 0.754 | 0.761 | 0.770 | 0.780 | 0.829 | 0.835 | 0.843 | 0.851 |
| 6 | 0.748 | 0.744 | 0.741 | 0.739 | 0.808 | 0.813 | 0.820 | 0.830 |
| 7 | 0.708 | 0.710 | 0.714 | 0.722 | 0.792 | 0.783 | 0.774 | 0.768 |
| 8 | 0.755 | 0.752 | 0.759 | 0.769 | 0.805 | 0.804 | 0.806 | 0.812 |
| 9 | 0.799 | 0.788 | 0.799 | 0.769 | 0.812 | 0.805 | 0.802 | 0.800 |
| 10 | 0.761 | 0.763 | 0.766 | 0.771 | 0.842 | 0.836 | 0.830 | 0.824 |

The graphs of curves (in 2-D) corresponding to the resultant linear deformation $u$ = ($L_c$, T) for $n_a$ = {0, 5, 10 and 15 years}; are graphically shown in fig. 21, while the corresponding graphs (in 3-D) are shown figs. 22-25.

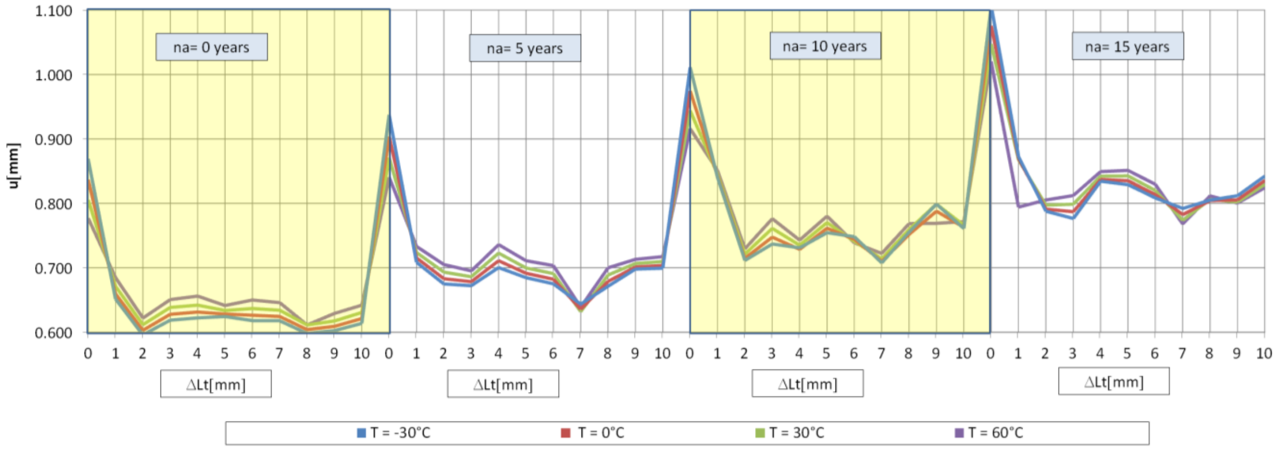


**Fig. 21.** The graphs of $u$ = ($L_c$, T) for: T = {-30 $^0$C, 0 $^0$C, 30 $^0$C, 60 $^0$C} and $n_a$= {0, 5, 10 and 15 years}

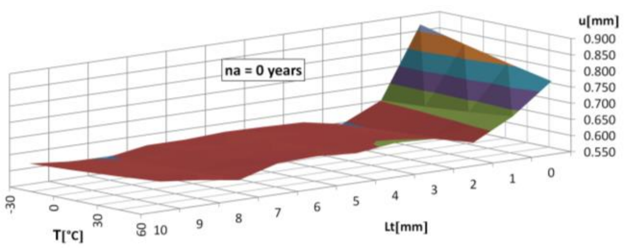


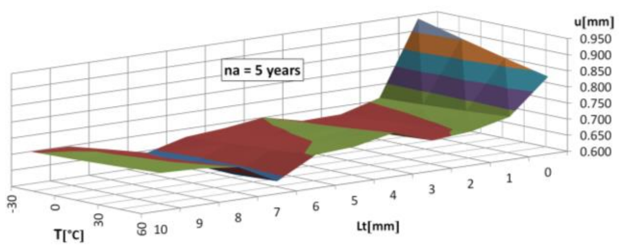


**Fig. 22.** The graphs of u ($L_c$, T) for $n_a$ = 0 years

**Fig. 23.** The graphs of u ($L_c$, T) for $n_a$ = 5 years

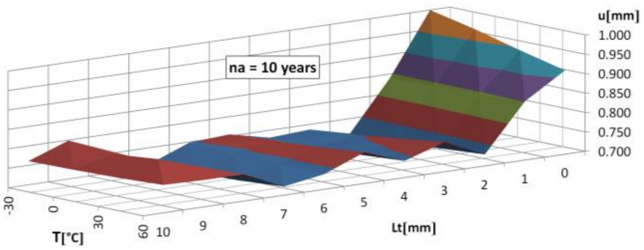


**Fig. 24.** The graphs of u = f($L_c$, T) for $n_a$ = 10 years

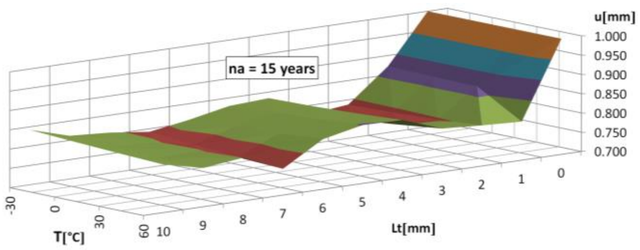


**Fig. 25.** The graphs of u = f($L_c$, T) for $n_a$ = 15 years

For the most important cases of the uniaxial traction loads, the resultant linear deformation *u* = ($L_c$, T) was calculated taking into account the results from table 3, while the corresponding graphs are shown in figs. 26-29.

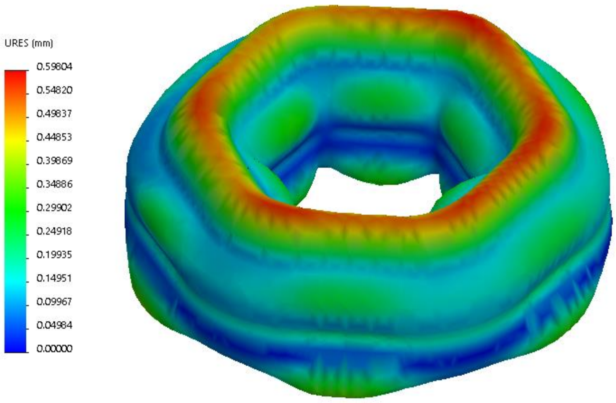


**Fig. 26.** The graphs of u = f($L_c$, T) for case 1

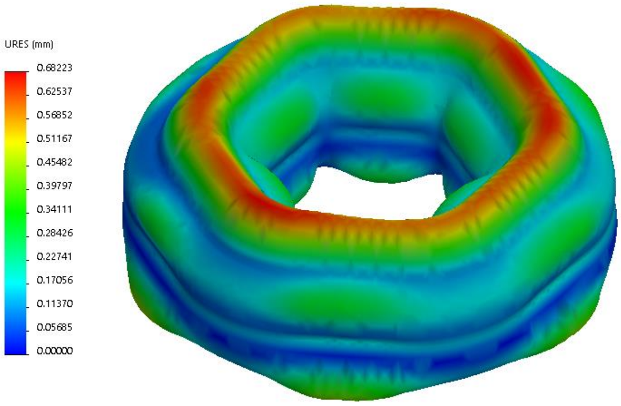


**Fig. 27.** The graphs of u = f($L_c$, T) for case 2

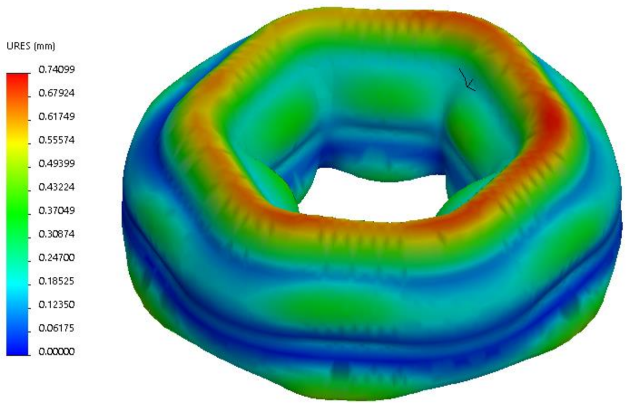


**Fig. 28.** The graphs of u = f($L_c$, T) for case 3

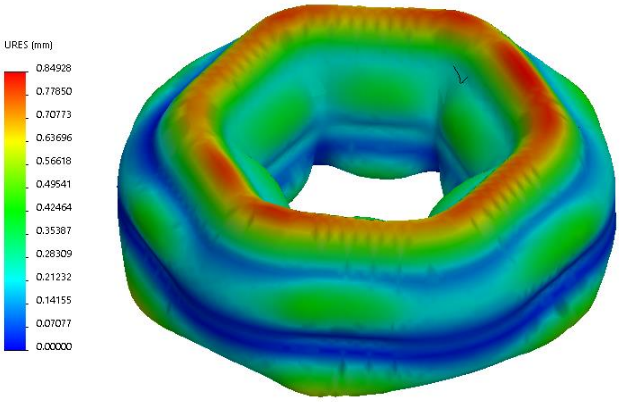


**Fig. 29.** The graphs of u = f($L_c$, T) for case 4

It was calculated the percentage variation of the resultant linear deformation Δu ($L_c$, T) versus the resulting state of the non-deformed tank (for $u_{Lc}$= 0), using the following formula:

$$\Delta u = \frac{(u_{Lc=0} - u)}{u_{Lc=0}} \cdot 100 \ [\%] \quad (2)$$

The percentage variation of resultant linear deformation Δu in relation to the initial value was calculated in table 5 and the corresponding graphs are given in fig. 30.

**Table 5:** The percentage variation of resultant liniar deformation Δu for $n_a$= 0, 5, 10 and 15 years

| Lc [mm] | T [⁰C] | | | | T [⁰C] | | | |
|---|---|---|---|---|---|---|---|---|
| | -30⁰ | 0⁰ | 30⁰ | 60⁰ | -30⁰ | 0⁰ | 30⁰ | 60⁰ |
| | $n_a$ = 0 [years] | | | | $n_a$ = 5 [years] | | | |
| | Δu [%] | | | | Δu [%] | | | |
| 1 | -25.02 | -21.16 | -16.65 | -11.88 | -24.42 | -20.84 | -16.90 | -12.79 |
| 2 | -31.45 | -27.95 | -24.06 | -19.95 | -28.01 | -24.42 | -20.39 | -16.13 |
| 3 | -28.82 | -24.98 | -20.73 | -16.26 | -28.30 | -24.93 | -21.21 | -17.30 |
| 4 | -28.41 | -24.55 | -20.29 | -15.56 | -25.30 | -21.33 | -17.00 | -12.45 |
| 5 | -28.17 | -24.93 | -21.32 | -17.45 | -26.97 | -23.48 | -19.65 | -15.42 |
| 6 | -28.90 | -25.15 | -20.94 | -16.35 | -27.99 | -24.50 | -20.65 | -16.32 |
| 7 | -28.92 | -25.37 | -21.27 | -16.87 | -31.35 | -29.66 | -27.43 | -23.98 |
| 8 | -31.19 | -27.82 | -24.12 | -21.33 | -28.39 | -24.88 | -20.90 | -16.73 |
| 9 | -30.69 | -27.21 | -23.35 | -19.03 | -25.55 | -22.40 | -18.85 | -15.17 |
| 10 | -29.40 | -25.77 | -21.71 | -17.38 | -25.40 | -22.15 | -18.51 | -14.67 |
| | $n_a$ = 10 [years] | | | | $n_a$ = 15 [years] | | | |
| | Δu [%] | | | | Δu [%] | | | |
| 1 | -16.92 | -13.58 | -10.45 | -7.07 | -21.14 | -19.16 | -17.17 | -22.15 |
| 2 | -29.64 | -26.65 | -23.59 | -20.35 | -28.78 | -26.46 | -23.88 | -21.06 |
| 3 | -27.11 | -23.28 | -19.36 | -15.25 | -29.80 | -26.83 | -23.73 | -20.39 |
| 4 | -27.70 | -25.23 | -22.13 | -18.88 | -24.57 | -22.17 | -19.57 | -16.75 |
| 5 | -25.38 | -21.86 | -18.41 | -14.82 | -25.06 | -22.35 | -19.54 | -16.56 |
| 6 | -25.99 | -23.63 | -21.49 | -19.34 | -26.92 | -24.37 | -21.71 | -18.68 |
| 7 | -30.01 | -27.16 | -24.37 | -21.14 | -28.39 | -27.24 | -26.13 | -24.72 |
| 8 | -25.28 | -22.84 | -19.54 | -16.09 | -27.22 | -25.22 | -23.01 | -20.44 |
| 9 | -20.99 | -19.15 | -15.36 | -16.04 | -26.60 | -25.12 | -23.43 | -21.55 |
| 10 | -24.74 | -21.73 | -18.85 | -15.76 | -23.84 | -22.32 | -20.79 | -19.19 |

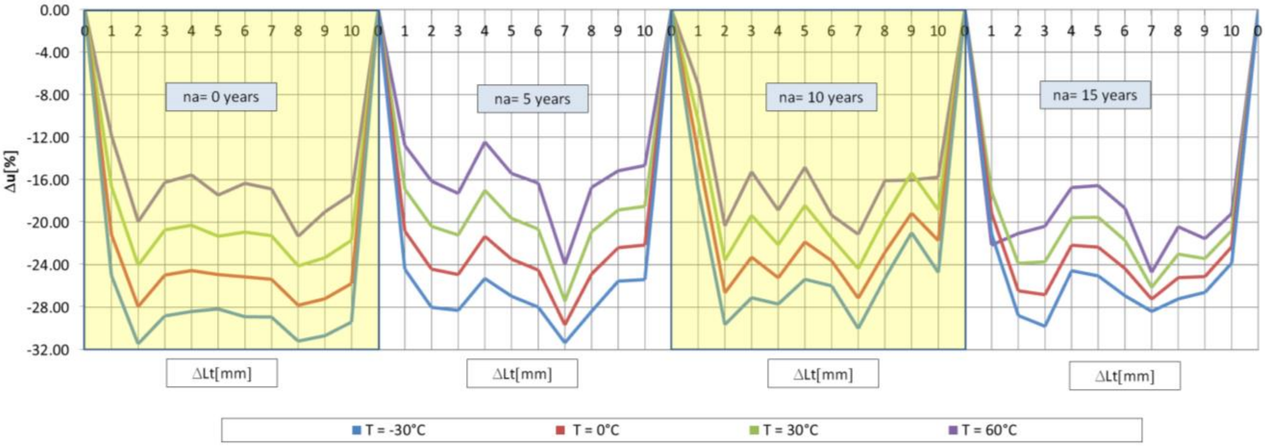


**Fig. 30.** The graphs of $\Delta u$ = ($L_c$, T) for: T = {-30 ⁰C, 0 ⁰C, 30 ⁰C, 60 ⁰C} and $n_a$= {0, 5, 10 and 15 years}

## 3. Conclusions

Following the numerical analyses and the resulting graphs it has been found that:
- for $n_a$= 15 years, $\sigma_{max}$ = 789.42 MPa > $\sigma_a$ = 710 MPa. Also, the state of efforts are amplified with the increase of corrosion and traction loads, and by the decreasing of the working temperature;
- the increase of the working temperature determines the decrease of the stress state, while the traction and corrosion process increase the stress state;

- $\Delta\sigma$ [%] ≅ 25.02% for T = 30 $^0$C and $n_a$= 10 years, while $\Delta\sigma$ [%] ≅ -24.02% for T = -30 $^0$C and $n_a$= 0 years;
- the highest values of resulting linear deformations and the Von Mises stress occur in the middle area of the torus sides. Also, the resultant linear deformation *u* is amplified with the increase of corrosion, traction loads, and the working temperature;
- $u_{max}$ ≅ 1.1 mm for T = -30 $^0$C and $n_a$= 10 years. $\Delta u_{max}$ [%] ≅ 31.45% for T = -30 $^0$C and $n_a$= 0 years;
- for $\Delta$L < 1.33% of the diameter of the torus, the stress state increases by $\Delta\sigma$ ≅ 25.02% and the percentage variation of resultant linear deformation $\Delta$u = 31.5%.

**References**

[1] Ghiţă, C. Mirela, Anton C. Micu, Mihai Ţălu, and Ştefan Ţălu. "Shape optimization of a thoroidal methane gas tank for automotive industry." *Annals of Faculty of Engineering Hunedoara - International Journal of Engineering,* Tome X, Fascicule 3 (2012): 295-297.
[2] Ghiţă, C. Mirela, Anton C. Micu, Mihai Ţălu, and Ştefan Ţălu. "Shape optimization of vehicle's methane gas tank." *Annals of Faculty of Engineering Hunedoara - International Journal of Engineering,* Tome X, Fascicule 3 (2012): 259-266.
[3] Ghiţă, C. Mirela, Anton C. Micu, Mihai Ţălu, Ştefan Ţălu, and Ema I. Adam. "Computer-Aided Design of a classical cylinder gas tank for the automotive industry." *Annals of Faculty of Engineering Hunedoara - International Journal of Engineering,* Tome XI, Fascicule 4 (2013): 59-64.
[4] Ghiţă, C. Mirela, Anton C. Micu, Mihai Ţălu, and Ştefan Ţălu. "3D modelling of a shrink fitted concave ended cylindrical tank for automotive industry." *Acta Technica Corviniensis – Bulletin of Engineering,* Tome VI, Fascicule 4 (2013): 87-92.
[5] Ghiţă, C. Mirela, Anton C. Micu, Mihai Ţălu, and Ştefan Ţălu. "3D modelling of a gas tank with reversed end up covers for automotive industry." *Annals of Faculty of Engineering Hunedoara - International Journal of Engineering,* Tome XI, Fascicule 3 (2013): 195-200.
[6] Ghiţă, C. Mirela, Ştefan C. Ghiță, Ştefan Ţălu, and Simona Rotaru. "Optimal design of cylindrical rings used for the shrinkage of vehicle tanks for compressed natural gas." *Annals of Faculty of Engineering Hunedoara - International Journal of Engineering,* Tome XII, Fascicule 3 (2014): 243-250.
[7] Bică, Marin, Mihai Ţălu, and Ştefan Ţălu. "Optimal shapes of the cylindrical pressurized fuel tanks." *Hidraulica Magazine*, no. 4 (December 2017): 6-17.
[8] Vintilă, Daniela, Mihai Ţălu, and Ştefan Ţălu. "The CAD analyses of a torospheric head cover of a pressurized cylindrical fuel tank after the crash test." *Hidraulica Magazine*, no. 4 (December 2017): 57-66.
[9] Ţălu, Ştefan, and Mihai Ţălu. "The influence of deviation from circularity on the stress of a pressurized fuel cylindrical tank." *Hidraulica Magazine*, no. 4 (December 2017): 34-45.
[10] Ţălu, Mihai. "The influence of the corrosion and temperature on the Von Mises stress in the lateral cover of a pressurized fuel tank." *Hidraulica Magazine*, no. 4 (December 2017): 89-97.
[11] Ţălu, Mihai, and Ştefan Ţălu. "Analysis of temperature resistance of pressurized cylindrical fuel tanks." *Hidraulica Magazine*, no. 1 (March 2018): 6-15.
[12] Ţălu, Mihai, and Ştefan Ţălu. "Design and optimization of pressurized toroidal LPG fuel tanks with variable section." *Hidraulica Magazine*, no. 1 (March 2018): 32-41.
[13] Ţălu, Ştefan, and Mihai Ţălu. "Algorithm for optimal design of pressurized toroidal LPG fuel tanks with constant section described by imposed algebraic plane curves." *Hidraulica Magazine*, no. 2 (June 2018): 14-21.
[14] Ţălu, Mihai, and Ştefan Ţălu. "The optimal CAD design of a 3D hexagonal toroid with regular hexagonal cross-section used in manufacturing of LPG storage tanks." *Hidraulica Magazine*, no. 2 (June 2018): 49-56.
[15] Ţălu, Mihai, and Ştefan Ţălu. "The influence of corrosion and temperature variation on the minimum safety factor of a 3D hexagonal toroid with regular hexagonal cross-section used in manufacturing of LPG storage tanks." *Hidraulica Magazine*, no. 3 (September 2018): 16-25.
[16] Ţălu, Ştefan, and Mihai Ţălu. "The influence of corrosion and pressure variation on the minimum safety factor of a 3D hexagonal toroid with regular hexagonal cross-section used in manufacturing of LPG storage tanks." *Hidraulica Magazine*, no. 3 (September 2018): 39-45.
[17] Ţălu, Mihai, and Ştefan Ţălu. "The influence of corrosion and temperature variation on a CNG storage tank with a combined form consisting of a torus and a sphere." *Hidraulica Magazine*, no. 4 (December 2019): 93-104.
[18] Ţălu, Mihai, and Ştefan Ţălu. "Optimal design of a CNG storage tank with a combined form consisting of a torus and a sphere." *Hidraulica Magazine*, no. 4 (December 2019): 73-82.
[19] Ţălu, Mihai, and Ştefan Ţălu. "Study of temperature–corrosion–torsion affecting factors on the shape of a toroidal LPG tank using the finite element method." *Hidraulica Magazine*, no. 1 (March 2020): 21-32.

[20] Ţălu, Ştefan, and Mihai Ţălu. "Numerical analysis of the influence of uniaxial compression loads on the shape of a toroidal LPG tank." *Hidraulica Magazine*, no. 1 (March 2020): 47-58.
[21] Ţălu, Mihai, and Ştefan Ţălu. "Stress and deformation analysis under bending and torsional loads of a toroidal LPG tank based on the finite element analysis." *Hidraulica Magazine*, no. 1 (March 2020): 88-101.
[22] Patel, Pankit, and Jaypalsinh Rana. "Design & optimization of LNG-CNG cylinder for optimum weight." *IJSRD - International Journal for Scientific Research & Development* 1, no. 2 (2013): 282-286.
[23] Oprițoiu, Petre. "Comparative study of the effect of the compression and traction loads on the stress and deformation of a toroidal LPG tank." *Hidraulica Magazine*, no. 2 (June 2021): 15-28.
[24] Ţălu, Mihai, and Ştefan Ţălu. "3D geometrical solutions for toroidal LPG fuel tanks used in automotive industry." *Advances in Intelligent Systems Research* 151 (2018): 189-193. DOI: 10.2991/cmsa-18.2018.44.
[25] Ţălu, Ştefan, and Mihai Ţălu. "Constructive CAD variants of toroidal LPG fuel tanks used in automotive Industry." *Advances in Intelligent Systems Research* 159 (2018): 27-30. DOI: 10.2991/mmsa-18.2018.7.
[26] Ţălu, Ştefan, and Mihai Ţălu. "The Influence of corrosion on the vibration modes of a pressurized fuel tank used in automotive industry." *DEStech Transactions on Materials Science and Engineering* (2018): 1-6. DOI: 10.12783/dtmse/icmsa2018/20560.
[27] Ţălu, Mihai, and Ştefan Ţălu. "Optimal engineering design of a pressurized paralepipedic fuel tank." *Annals of Faculty of Engineering Hunedoara - International Journal of Engineering,* Tome XVI, Fascicule 2 (2018): 193-200.
[28] Ţălu, Ştefan, and Mihai Ţălu. "CAD generating of 3D supershapes in different coordinate systems." *Annals of Faculty of Engineering Hunedoara - International Journal of Engineering,* Tome VIII, Fascicule 3 (2010): 215-219.
[29] Ţălu, Ştefan, and Mihai Ţălu. "A CAD study on generating of 2D supershapes in different coordinate systems." *Annals of Faculty of Engineering Hunedoara - International Journal of Engineering,* Tome VIII, Fascicule 3 (2010): 201-203.
[30] Oprițoiu, Petre. "Analysis of stresses and displacements in the deformed bent 3D hexagonal toroid with regular hexagonal cross-section used in manufacturing of lpg storage tanks." *Hidraulica Magazine*, no. 2 (June 2020): 15-26.
[31] Ţălu, Ştefan. *AutoCAD 2017*. Cluj-Napoca, Napoca Star Publishing House, 2017.
[32] Oprițoiu, Petre. *Research on heat transfer and pressure losses through porous metal heat exchanger / Cercetări privind transferul termic și a pierderilor de presiune la un schimbător de căldură din metal poros.* PhD thesis, Technical University of Cluj-Napoca, Romania, Faculty of Mechanics, 2014.
[33] Oprițoiu, Petre. "Fluid flow and pressure drop simulation in aluminium foam heat exchanger." *Acta Technica Napocensis: Civil Engineering & Architecture*, no. 50 (2007): 101-112.
[34] Oprițoiu, Petre. "Heat transfer performance analysis in porous heat exchanger." *Hidraulica Magazine*, no. 3 (September 2015): 32-41.
[35] Oprițoiu, Petre. "Rans simulation of combined flow and heat transfer through open-cell aluminum foam heat sink." *Hidraulica Magazine*, no. 3 (September 2013): 15-25.
[36] Oprițoiu, Petre. "Prediction of turbulent flow using upwind discretization scheme and k-ε turbulence model for porous heat exchanger." *Hidraulica Magazine*, no. 2 (June 2016): 88-97.
[37] Oprițoiu, Petre. "Validation of porous heat exchanger simulation model." Paper presented at 21st International Conference and Exhibition of Hydraulics and Pneumatics HERVEX 2014, Călimănești-Căciulata, Romania, November 5-7, 2014.